NANO · MICRO small
www.small-journal.com

Simulations of the Oxidation and Degradation of Platinum Electrocatalysts

Björn Kirchhoff, Laura Braunwarth, Christoph Jung, Hannes Jónsson, Donato Fantauzzi, and Timo Jacob**

Improved understanding of the fundamental processes leading to degradation of platinum nanoparticle electrocatalysts is essential to the continued advancement of their catalytic activity and stability. To this end, the oxidation of platinum nanoparticles is simulated using a ReaxFF reactive force field within a grand-canonical Monte Carlo scheme. 2–4 nm cuboctahedral particles serve as model systems, for which electrochemical potential-dependent phase diagrams are constructed from the thermodynamically most stable oxide structures, including solvation and thermochemical contributions. Calculations in this study suggest that surface oxide structures should become thermodynamically stable at voltages around 0.80–0.85 V versus standard hydrogen electrode, which corresponds to typical fuel cell operating conditions. The potential presence of a surface oxide during catalysis is usually not accounted for in theoretical studies of Pt electrocatalysts. Beyond 1.1 V, fragmentation of the catalyst particles into $[Pt_6O_8]^{4-}$ clusters is observed. Density functional theory calculations confirm that $[Pt_6O_8]^{4-}$ is indeed stable and hydrophilic. These results suggest that the formation of $[Pt_6O_8]^{4-}$ may play an important role in platinum catalyst degradation as well as the electromotoric transport of $Pt^{2+/4+}$ ions in fuel cells.

1. Introduction

Platinum-based nanoparticulate electrocatalysts are currently the most widely used oxygen reduction catalysts in various fields of application, for example, metal–air batteries,[1] plasma catalysis,[2] or polymer–electrolyte membrane fuel cells.[3] Given the socioeconomic implications of precious metal mining, it is necessary to optimize the performance of these materials as much as possible if widespread deployment of fuel cell technology is to become reality. To this end, extending the lifetime of Pt electrocatalysts by minimizing material degradation[4] and Pt loading[5] as well as increasing their activity toward the cathodic oxygen reduction reaction (ORR) are paramount objectives. Alloying with nonplatinum-group metals has proved to be a successful avenue.[6] Similarly, varying the shape of the nanoparticle (NP) catalyst can expose different types of surface facets, edges, kinks, and other lower coordinated sites, which govern reactivity and selectivity.[7–11] Computational methods have played an integral part in these efforts for predicting catalysts with improved ORR performance. For instance, the density functional theory (DFT)–based screening approach utilized by Nørskov et al. has, in particular, turned out to be useful.[12–14] There, trends for free energy changes of the ORR intermediates are investigated on pristine, infinite surface model systems with the goal of identifying bottleneck steps and to suggest chemical or structural modifications to overcome them. However, some studies have called into question whether such model systems are in fact representative of the structure of fuel cell catalysts under working conditions.[15,16] In a combined theoretical–experimental study, our group has recently shown that stable surface oxides do exist on single-crystalline Pt(111) at near-ambient pressure and have potential impact on its electrocatalytic behavior.[16] Similarly, a DFT study by Seriani et al. has indicated that a few layers of Pt_3O_4 are thermodynamically stable on a Pt(100) surface and are catalytically active toward methane dissociation.[15] Clearly, more research into the influence of surface oxides on catalysis is needed to improve the catalytic activity of these materials.

In the present work, a grand-canonical Monte Carlo (GCMC)[17,18] algorithm is used in combination with a ReaxFF[19] reactive force field to investigate the oxidation of Pt

B. Kirchhoff, Prof. H. Jónsson, Dr. D. Fantauzzi
Science Institute and Faculty of Physical Sciences
University of Iceland
107 Reykjavík, Iceland
E-mail: donato@hi.is

B. Kirchhoff, L. Braunwarth, Prof. T. Jacob
Institute of Electrochemistry
Ulm University
Albert-Einstein-Allee 47, 89081 Ulm, Germany
E-mail: timo.jacob@uni-ulm.de

C. Jung, Dr. D. Fantauzzi, Prof. T. Jacob
Helmholtz Institute Ulm (HIU) Electrochemical Energy Storage
Helmholtz-Straße 16, 89081 Ulm, Germany

C. Jung, Dr. D. Fantauzzi, Prof. T. Jacob
Karlsruhe Institute of Technology (KIT)
P.O. Box 3640, 76021 Karlsruhe, Germany

The ORCID identification number(s) for the author(s) of this article can be found under https://doi.org/10.1002/smll.201905159.

DOI: 10.1002/smll.201905159

nanoparticles. The computational models are 2–4 nm cuboctahedral particles, corresponding to the typical size range of catalysts used experimentally in fuel cells.[5] Note that particles larger than 4 nm become computationally too expensive to simulate within this scheme, and smaller particles could potentially be outside the confidence region of the force field description, as will be discussed in the following text. The thermodynamically most stable oxide structures are identified and energetics are further refined by considering stabilization through explicit solvation and thermochemical contributions obtained with the two-phase thermochemistry (2PT)[20] method. A potential-dependent phase diagram is constructed using the extended ab initio thermodynamics (EAITD)[21] approach. We find that oxidation of Pt NP catalysts starts at edges and vertices of the nanoparticle, with (111) facets showing surprising resistance toward oxidation. Surface oxide structures are predicted to be stable between ≈0.8 and 1.1 V versus standard hydrogen electrode (SHE), which coincides with typical fuel cell operating conditions. This result suggests that clean metal surfaces might not be appropriate model systems for Pt oxidation catalysts, for instance, ORR electrocatalysts under steady-state conditions. Upon complete oxidation, we observe dismemberment of the particle into subunits of Pt_6O_8 stoichiometry. DFT calculations confirm the high stability and hydrophilicity of these $[Pt_6O_8]^{4-}$ units. Thus, we propose that $[Pt_6O_8]^{4-}$ could be responsible for the transport of ionic Pt species through the fuel cell and thereby plays an important role in fuel cell catalyst degradation.

2. Results and Discussion

The reactive force field developed in-house used in this study was initially trained for surface science applications.[22] Focusing on oxidation processes on Pt(111), it was successfully employed to reveal the importance of surface-buckled and subsurface oxide structures[23] and to predict the growth of stable surface oxides under near-ambient pressure, which was then validated by in situ X-ray photoelectron spectroscopy (XPS).[16] However, transferability of the force field to nanoparticulate systems needs to be confirmed. To this end, two tests are performed. First, we examine the stability of octahedral (only (111) facets), cubic (only (100) facets), dodecahedral (only (110) facets), cuboctahedral (both (111) and (100) facets), and spherical (mixed facets) particles in the catalytically relevant size range between ≈1 and 10 nm. **Figure 1** depicts the dependence of the energy per atom, E_{atom}, on the number of atoms in the particle. The stability sequence resulting from Figure 1 is cuboctahedron > octahedron > sphere > dodecahedron > cube, with the spherical particle somewhat increasing in stability above 3 nm. This sequence is in good agreement with results from studies using quantum-corrected Sutton–Chen type potentials[24–26] and is consistent with DFT calculations for single crystal surfaces of the same Miller indices (constituting the corresponding NPs).[22] Note that for increasing particle sizes, E_{atom} values converge toward the fcc-Pt cohesive energy obtained with the present force field (E_C = 5.77 eV per atom; experimental: 5.84 eV per atom[27]). In a second test, the force field's performance for smaller particles is explored. To this end, we reproduce a recently published DFT study on the formation energy of Pt clusters by Lambie et al.[28] with our force field.

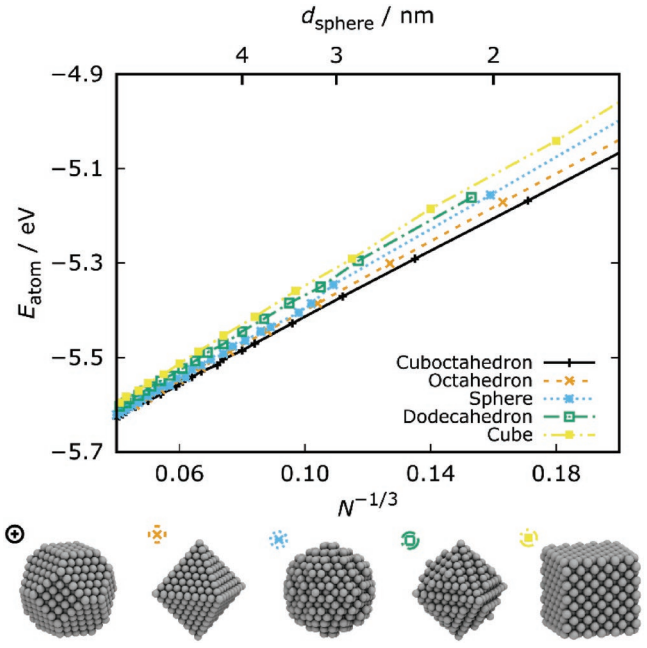

Figure 1. Stability of cuboctahedral, octahedral, spherical, dodecahedral, and cubic NPs as a function of particle size. *N*: number of atoms in a particle. The key diameter of the spherical particle, d_{sphere}, is given on top. Bottom: illustration of NP structures of ≈3 nm size.

The results are shown and discussed in more detail in Figure S1 (Supporting Information). Combining this finding with results for nanoparticles with extended facets (see Figure 1), we can conclude that the force field is appropriate for simulations of small (<100 atoms) and larger nanoparticles (≳3 nm).[5] For the intermediate particle size range, the comparison shows an error in the formation energy in the range of 0.1–0.3 eV per atom. Therefore, emphasis is placed on the 3 nm particle (711 atoms, see Figure 1).

An in-depth description of the GCMC algorithm can be found in refs. [14] and [15]. Conditions are chosen by adjusting the chemical potential μ_O of the oxygen reservoir, which is a function of temperature T and oxygen partial pressure p_O. In the present study, isobaric oxidation is investigated at ultra-high vacuum (UHV, $p_O = 10^{-10}$ mbar) and near-ambient pressure (NAP, p_O = 1 mbar) in the temperature range between 200 and 1400 K. NAP conditions are considered following our recent combined theoretical–experimental effort that made use of NAP–XPS spectroscopy to investigate oxidation of Pt(111).[16]

Figure 2 illustrates examples of the most stable structures obtained with the ReaxFF–GCMC approach under NAP conditions. The oxygen-to-platinum ratio, x_O, is used to quantify the degree of oxidation.[18,29] At 1250 K and beyond, an adsorbate-free state is thermodynamically favored. As the temperature decreases, oxidation starts at vertices and edges of the NP while the overall shape is still retained. x_O increases slowly in this regime, which will be referred to as surface adsorption. The first significant jump in coverage is observed at 950 K. At this temperature and below, edges and vertices are densely covered and oxidation proceeds to the (100) facets of the cuboctahedral particle. Notably, oxygen coverage on (111) facets remains low during this stage. Cross-sections of structures at this temperature reveal that oxidation

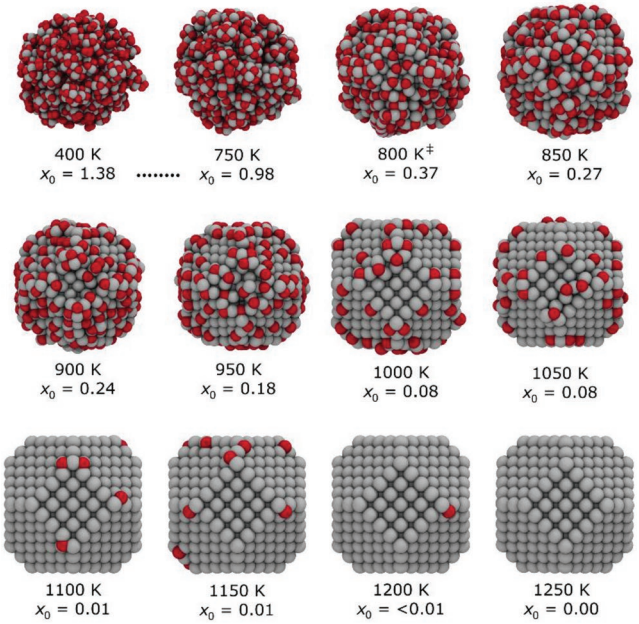

Figure 2. Overview of the oxidation process. Thermodynamic equilibrium structures from the isobaric oxidation process of a 3 nm cuboctahedral particle at p_O = 1 mbar. x_O: oxygen-to-platinum ratio. ‡ Below 800 K, complete oxidation of the particle is observed.

has not proceeded to the core of the particle but is confined to only a few surface layers, analogous to our recent observations for Pt(111).[16] This regime will therefore be referred to as surface oxide. Complete oxidation of the particle is first observed at 750 K, indicated by a jump of x_O to ≈1.0. Notably, these fully oxidized structures are dominated by a motif of smaller subunits of Pt_6O_8 stoichiometry. To the best of our knowledge, this observation is unprecedented and will be discussed in more detail below. As temperature decreases further, x_O increases up to ≈1.4 at 400 K. The same Pt_6O_8 motif is observed throughout, however, an additional motif appears where particles are decorated with dioxygen species. Under UHV conditions, similar structures are generated, albeit shifted to lower temperature with respect to NAP (see Figure S2 in the Supporting Information). This indicates that thermodynamic equilibrium was reached in all cases.

To develop a better understanding of the electrochemical stability of these different oxide structures, potential-dependent phase diagrams are constructed using the EAITD approach.[21] To represent the adsorbate-free system, we consider two models: i) the perfectly ordered cuboctahedral nanoparticle ("pristine"), which was also the input structure for our GCMC simulations, and ii) a slightly disordered particle ("rearranged") generated by removing O atoms from a surface-oxidized structure and subsequent structural relaxation. The rearranged system is expected to be a more realistic representation of the catalyst's structure than the pristine (perfect) system considering the stresses acting on the particle due to repeated reductive jumps and the thermal discharge generated by the ORR on the particle surface. The latter can cause local surface melting which was recently observed for Cu NPs to occur significantly below the actual melting temperature.[30] To lend more significance to the rearranged model, in the following text, all values are averaged over 5 different particles, generated from initially oxidized structures with x_O = 0.1–0.5. Note that particles with $x_O > 0.5$ typically contain the Pt_6O_8 motif and will lead to highly disordered structures that are significantly less stable in comparison to the pristine cluster. To identify the most stable oxidized structures, all particles generated during GCMC sampling are first grouped based on their x_O. Bins of Δx_O = 0.1 and 0.01 were tested and it was found that no important information is lost in case of the coarser division. From within each of these groups, the structure with the lowest formation energy (E_F) is determined. The structures found this way are then introduced into a simulation box filled with water molecules at a density of ρ_{H_2O} = 1.0 g cm^{-3}. Afterward, reactive molecular dynamics (MD) simulations are run at 300 K (*NVT* ensemble) for 500 000 iterations (Δt = 0.25 fs). E_{solv} is then obtained by averaging over the latter 250 000 iterations. Results are summarized in **Table 1**.

Several noteworthy trends are observed for E_{solv}. First, the solvation energy for the pristine system is larger than for surface-oxidized structures (x_O = 0.1–0.4). This trend likely results from oxygen atoms at the surface breaking up the regular ordering of solvent molecules in comparison to the pristine particle. **Figure 3**a,b illustrates the first solvation shell around the pristine particle. The arrangement of water molecules observed here is akin to reports of a hydrophobic water monolayer on Pt(111).[31] Note that additionally to H_2O, a small amount of H and OH adspecies are formed during these simulations. While the rearranged particle is also slightly more stabilized by the water environment than the surface-oxidized systems, the calculated solvation stabilization is considerably lower (≈25%) than for the pristine system. The ordering of H_2O molecules on its surface is more irregular than in the case of the pristine particle, see Figure 3c. At larger x_O, solvation stabilization is larger than for the clean system. This can be attributed to the increased hydrophilicity of these structures. Entropic contributions S are obtained using the 2PT.[20] To this end, *NVE*-ensemble MD simulations are carried out at an initial temperature of 300 K starting with the structures without solvent for

Table 1. Summary of solvation energy values (E_{solv}), entropic (S) corrections, and final formation free energy values (ΔG_F). "Pristine" and "rearranged" refer to a perfect cuboctahedron and a slightly rearranged particle, see Figure 4. Values for the rearranged cluster are an average over 5 systems (see text).

Structure	E_{solv}[a)] [eV]	TS[b)] [eV]	ΔG_F [eV]@0 V[c)]
Pristine	−94.18	−83.61	0.00(reference)
Rearranged	−76.04	−84.51	13.26
x_O = 0.1	−66.19	−91.63	90.79
x_O = 0.2	−68.82	−96.01	219.42
x_O = 0.4	−86.34	−33.53	514.93
x_O = 1.1	−128.16	−133.94	1659.04

[a)]Obtained from MD simulations (*NVT* ensemble) at 300 K and a density of explicit solvent molecules of ρ_{H_2O} = 1.0 g cm^{-3}; [b)]2PT results from MD simulations (*NVE* ensemble) with a starting temperature of 300 K; [c)]All values calculated against H_2/H_2O at standard conditions (pH 0, T = 298 K, p = 1 bar) and the pristine cluster as reference.

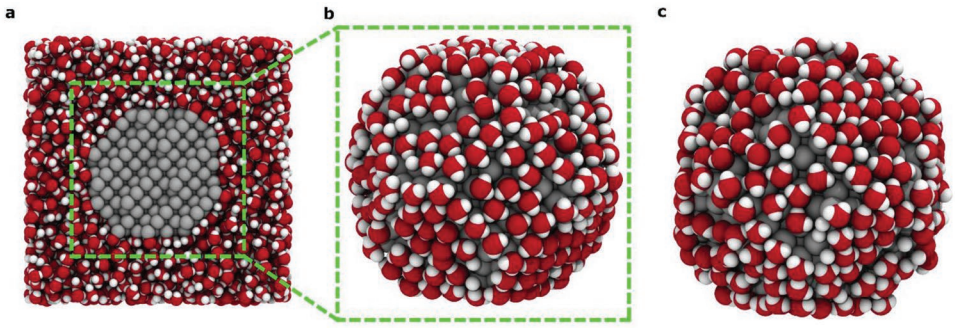

Figure 3. Solvated particles. a) Solvated pristine particle in water (shown is a cut through the simulation box). b,c) First layer of H_2O solvent molecules on the pristine (b) and rearranged particle (c). All snapshots from MD simulations.

13.8 ps from which the last 1.3 ps are used to evaluate entropy contributions with the 2PT approach. As summarized in Table 1, *S* is found to increase as particles become more disordered either due to rearrangement or oxidation of the particle. Formation free energy values of the most stable structures that entered the phase diagram are also summarized in Table 1.

Figure 4 shows the calculated oxidation phase diagrams for the 3 nm cuboctahedral particle. This phase diagram includes the solvation energy and entropic contributions discussed earlier; phase diagrams without solvation or entropic contributions data are shown in Figure S3 (Supporting Information). Approximately 500 000 structures were generated using GCMC simulations, and they were grouped with respect to x_O ($x_O = 0.1$–1.5, $\Delta x_O = 0.1$). For clarity, only the most stable structures—i.e., the enveloping, lowest-energy lines that define the phases by their intersections—are shown. In Figure 4, the stability of the oxidized structures is referenced against the rearranged particle and not the ideal, defect-free system since the latter are unlikely to exist under experimental conditions and after repeated oxidation and reduction cycles. Three overall regions can be distinguished. First, in the range between 0.00 and 0.80 V versus SHE, the adsorbate-free system is thermodynamically favored. From 0.80 to 0.85 V onward, which corresponds to typical fuel cell operating conditions, surface oxide structures are starting to become the thermodynamically preferred phase. This also coincides well with the experimentally observed onset of platinum oxidation in nonadsorbing solvents in cyclic voltammograms.[32] Without solvation and entropic contributions, this phase transition is shifted to slightly lower potentials, see Figure S3 in the Supporting Information. Beyond 1.15 V, the simulations predict full oxidation of the particle. Note that for 2 and 4 nm particles, the onset of full oxidation is shifted by −270 and +100 mV, respectively, indicating that this process is size-dependent (see Figure S3 in the Supporting Information). On the other hand, the onset of surface oxide formation is found to be shifted by −100 mV for the 2 nm particle but is identical for the larger 4 nm particle. Generally, the surface oxide window becomes larger with particle size. Finally, a comparison of phase diagrams without (Figure S3, Supporting Information) and with thermochemical corrections (Figure 4) of the 3 nm particle shows that inclusion of entropy and solvation leads to a slight shrinkage of the surface oxide phase. This is likely a result of solvation stabilizing the clean and fully oxidized systems more strongly than the surface-oxidized structures.

The second major observation in this work concerns the Pt_6O_8 units present in fully oxidized structures. Pt_6O_8 can be described as Pt icosahedron inside a cube of oxygen atoms.[33] Stoichiometrically, this structure should be derived from the Pt_3O_4 phase. However, some key differences can be observed when comparing the two structures as presented in Table S1 (Supporting Information). Most notably, only one type of

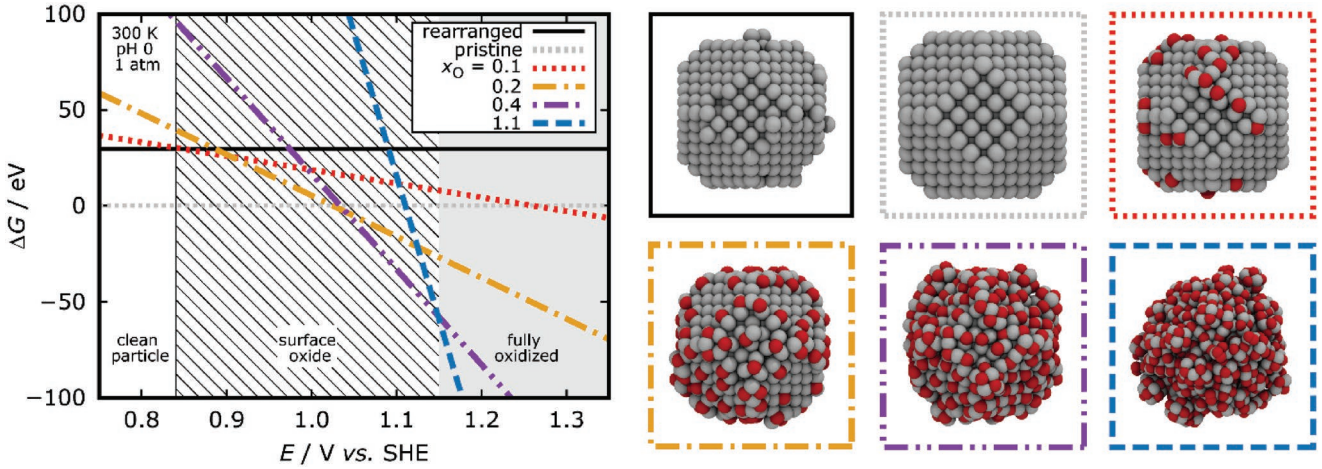

Figure 4. Potential-dependent phase diagram for a 3 nm cuboctahedron and illustration of the thermodynamically most stable structures therein.

Pt—O bond is found in Pt_6O_8, while Pt_3O_4 features two types of inequivalent Pt—O bonds. This assessment is supported by a comparison of calculated partial charge distributions of a fully oxidized nanoparticle from GCMC and spherical particles cut from PtO, α-PtO_2, β-PtO_2, and Pt_3O_4 crystals (see Figures S4 and S5 in the Supporting Information). Pt_6O_8 has been discussed by Vegas to most likely correspond to a mixed-valence compound of 4 Pt(IV) and 2 Pt(II) with four net negative charges in the context of explaining the crystal structure of Pt_3O_4.[33] We will thus refer to it as $[Pt_6O_8]^{4-}$. To the best of our knowledge, so far the only experimental report mentioning this species is a thesis work by Dimas Rivera, who observed an interlattice distance corresponding to the (012) plane of Pt_6O_8 using high-resolution transmission electron microscopy on a composite Pt–Fe/Al_2O_3 hydrogenation catalyst.[34] It is unsurprising that $[Pt_6O_8]^{4-}$ has so far not been observed in experiments due to the necessity for intricate operando studies and because this kind of degradation product has simply not been considered and expected so far. While experimental confirmation is needed to establish $[Pt_6O_8]^{4-}$ as a primary degradation product of Pt-based electrocatalysts, theoretical evidence will now be presented in favor of the significance of this observation. As a first clue, note that although our force field had not been trained to directly reproduce the Pt_3O_4 phase, the formation of these Pt_6O_8 units could still be observed, indicating a remarkably high driving force for its formation.

Afterward, the $[Pt_6O_8]^{4-}$ cluster is studied more closely by DFT. Molecular DFT calculations of $[Pt_6O_8]^n$ ($n = 0, -2, -4, -6$) in various spin states are summarized in Table S2 (Supporting Information); they reveal that $^1[Pt_6O_8]^{4-}$ is indeed, as suggested by Vegas, the most stable combination of spin and charge state when a stabilizing water environment is taken into account. The formation energy from the elements is exothermic. A similar result is obtained in periodic DFT calculations. DFT results are therefore in good agreement with ReaxFF calculations regarding the stability and ease of formation of the $[Pt_6O_8]^{4-}$ cluster. See the Experimental Section and Supporting Information for more information on these calculations.

Finally, in order to evaluate their influence on particle degradation, we study the detachment of Pt_6O_8 clusters from a fully oxidized particle using ReaxFF. There is an endothermic energy difference of ≈1.6 eV between the particle with an attached Pt_6O_8 cluster and the cluster dissociated from the nanoparticle. This result is unsurprising due to the instability of anions in the gas phase.[35] It is therefore important to take into account the influence of the solvent on this process. To this end, we perform MD calculations of the nanoparticle in the solvent, see Figure S6 (Supporting Information). The initial state of this simulation, showing the solvated nanoparticle with the Pt_6O_8 motif, is illustrated in **Figure 5**. We find that when being solvated, detachment of the Pt_6O_8 cluster is now exothermic by ≈11–12 eV, which is in good agreement with the high stabilization computed using DFT with implicit solvent models.

Based on these results, we offer the hypothesis that $[Pt_6O_8]^{4-}$ could not only be involved in the catalyst's degradation process but also in the transport of $Pt^{2+/4+}$ ions through the fuel cell. The mechanism of propagation would be similar to what was proposed by Guilminot et al.,[36] who analyzed a proton exchange membrane fuel cell using a Pt/C catalyst after 529 h of continuous operation and reported the presence of Pt^{2+} and Pt^{4+} in the electrolyte. They argue that these ions form anionic complexes with halide impurities that originate from catalyst synthesis and experience electromotoric drag that moves them throughout the cell. However, we suggest that $[Pt_6O_8]^{4-}$ is the active species in this mechanism based on the calculated properties of this cluster. Certainly, more experimental evidence is required to assess this hypothesis. It must also be stressed that, given the nature of the GCMC approach, all results presented here describe the thermodynamic behavior, while kinetic aspects—as for instance, activation barriers related to the formation of the Pt_6O_8 units—are not included. However, the presented studies provide an important basis for further studies on these interesting effects.

3. Conclusion

To summarize, a potential-dependent electrochemical phase diagram is constructed from the thermodynamically most stable oxide structures found for 2–4 nm cuboctahedral nanoparticles using the ReaxFF–GCMC approach. Gas-phase formation energy values from GCMC are further refined by considering explicit water solvation and entropic corrections. The resulting phase diagram predicts the existence of stable surface oxides at electrochemical potentials between ≈0.8 and 1.1 V versus SHE. Additionally, a degradation mechanism involving anionic units of Pt_6O_8 stoichiometry is reported. Formation of $[Pt_6O_8]^{4-}$ is found to be exothermic both in DFT and ReaxFF calculations and the molecule appears to be hydrophilic. Detachment of a Pt_6O_8 cluster from the oxidized particle is found to be exothermic under aqueous conditions. We propose this structure to be a primary and important oxidation product of Pt NP electrocatalysts and to be involved in Pt nanoparticle degradation as well as the electromotoric transport of $Pt^{2+/4+}$ ions in fuel cells.

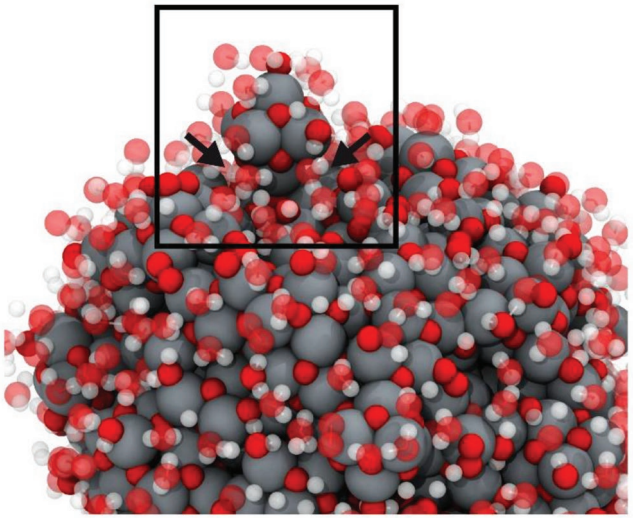

Figure 5. Fully oxidized Pt nanoparticle containing the Pt_6O_8 motif shown with a selection of solvent molecules. The rectangular box highlights a Pt_6O_8 unit where arrows indicated the "attack" by solvent molecules, potentially assisting detachment of solvated $[Pt_6O_8]^{4-}$.

4. Computational Section

The freeware python 3 program nanocut[37] was used to cut nanoparticles from a fcc-Pt crystal. Lattice parameters for fcc-Pt as well as for the tested Pt oxides optimized using ReaxFF are listed in Table S3 (Supporting Information). ReaxFF–GCMC calculations were performed using the implementation of ReaxFF by software for chemistry & materials (SCM) in the Amsterdam Density Functional Suite Version 2017.106[19,38,39] and the GCMC algorithm by Senftle et al.[17,18] In short, the algorithm would randomly choose to insert, delete, or move an oxygen atom in the simulation box while the number Pt atoms was kept constant ($\mu_O N_{Pt} VT$ ensemble, where μ_O is the chemical potential of the oxygen reservoir). The geometry of the newly generated structure was then relaxed within the ReaxFF framework and accepted or dismissed based on the energy criterion. As ReaxFF followed a bond-order representation of the energy terms, it allowed for bond formation or breakage, thereby enabling structural rearrangement during relaxation cycles. Formally, this process was repeated until equilibrium with the gas phase reservoir reached. In practice, however, the GCMC algorithm was implemented with a forward bias, which pushed the simulation beyond the point of equilibrium in order to facilitate sampling of local minima. Careful postanalysis of all structures generated along the way was therefore required to find the minimum energy structure under the given simulation conditions. The Pt—O—H force field developed in the group was used.[22] Initial geometry optimizations of the nanoparticle structures used a convergence criterion of 0.05 kcal mol^{-1}. Up to 1000 energy relaxation steps were performed in between the GCMC steps, using a convergence criterion of 0.5 kcal mol^{-1}. A bond order cutoff of 0.0075 was employed, as well as full system electronegativity equalization method (EEM) charge equilibration. GCMC simulations usually achieved convergence within ≈30 000 iterations. Solvation energy calculations were carried out by placing the NP in a simulation box filled with explicit water molecules (≈5000 molecules, depending on the system), maintaining a density of ρ_{H_2O} = 1.0 g cm^{-3}. Simulations were carried out for 500 000 iterations using a time step of 0.25 fs and a temperature damping constant of 100 fs with the Velocity–Verlet algorithm and Berendsen thermostat (*NVT* ensemble). E_{solv}^{system} was obtained from the latter 250 000 iterations and was calculated according to Equation (1) as

$$E_{solv}^{system} = E^{system}(aq) - E^{system} - N_{H_2O} \cdot E_{tot}^{H_2O} \quad (1)$$

where $E^{system}(aq)$ is the total energy of the solvated particle, E^{system} is the total energy of the particle from GCMC calculations, N_{H_2O} is the number of H_2O molecules in the simulation box, and $E_{tot}^{H_2O}$ is the averaged total energy of a water molecule. The water density (not the number of water molecules) was kept constant at ρ_{H_2O} = 1.0 g cm^{-3}. For the 2PT analysis, particles were equilibrated for 55 000 iterations in an *NVE* ensemble with a starting temperature of T = 300 K and the same time step as before. The last 5000 iterations were used for the analysis. Enthalpy and entropy corrections for the oxygen molecule corrections (obtained from the thermochemical tables of the National Institute of Standards and Technology and the Joint Army-Navy-NASA-Air Force Interagency Propulsion Committee (NIST-JANAF)) were used to obtain chemical potentials of O, H_2, and H_2O. Free energy G^{system} and potential-dependent formation free energy values $\Delta G_F^{system}(\Delta\phi)$ of the system under investigation were calculated according to Equations (2) and ((3)) as

$$G^{system} = E_{tot}^{system} + E_{solv}^{system} - TS^{system} \quad (2)$$

$$\Delta G_F^{system}(\Delta\phi) = G^{system} - G^{ref} - N_O\,\mu_O + 2e\Delta\phi \quad (3)$$

where E_{tot}^{system} is the total ReaxFF energy of the system from GCMC calculations, E_{solv}^{system} is the solvation correction obtained from MD simulations, T is the temperature, S^{system} is the entropic contribution obtained with the 2PT method, G^{ref} is the total free energy of the pristine cuboctahedral particle used as reference, N_O is the number of oxygen atoms in the system, μ_O is the chemical potential of oxygen (where $\mu_O = \mu_{H_2O} - \mu_{H_2}$), and e is the elementary charge. The last term of Equation (3) implied that in the electrochemical system all oxygen that was used for the Pt oxidation originated from a water splitting reaction. Detachment of the Pt_6O_8 cluster in a water environment was investigated using ReaxFF constrained-MD calculations; see the Supporting Information for detailed simulation procedure.

Periodic DFT calculations were performed with the Vienna Ab Initio Simulation Package (VASP)[40–43] using the projector-augmented wave method[44] to represent the basis set. The exchange-correlation functional by Perdew, Burke, and Ernzerhof (PBE) was used.[45] Plane waves were cut off at 350 eV. Wave functions were optimized to an accuracy of 10^{-6} eV, while forces were relaxed to below 10^{-2} eV Å^{-1}. Gaussian smearing with a smearing parameter of 0.001 eV was used. For implicit solvation calculations, the GLSSA13 solvent model[46] implemented in VASPsol was invoked[47–49] with the empirical bulk dielectric constant of water at room temperature (ε_{bulk} = 78.4). VASPsol implicitly located counterions in the double layer in a Poisson–Boltzmann-based approach. For this charge screening, a Debye length κ of 3.0 Å, which corresponded to a 1:1 electrolyte at pH 0 and concentration 1 M, was used. Molecular DFT calculations were performed using the ORCA software[50] using the same PBE exchange-correlation functional. Here, triple-ζ def2-TZVP basis sets[51] and def2/J auxiliary basis[52] in order to profit from the computational speedup provided by the resolution-of-identity approximation were used. Further, effective core potentials by Andrae et al. were employed for Pt.[53] Wave functions were optimized using the "TightSCF" setting. The conductor-like polarizable continuum solvation model (CPCM) used in conjuction with the solvent model based on density (SMD)[54] with standard settings for the water solvent was used in ORCA. The program *VMD* was used to visualize structures.[55]

Supporting Information

Supporting Information is available from the Wiley Online Library or from the author.

Acknowledgements

B.K. thanks the University of Iceland Research Fund for support through a PhD fellowship, Dr. Anna Garden for access to nanoparticle DFT structures, and Marcos Tacca for translation help of Spanish primary literature. Andrey Sinyavskiy is acknowledged for implementing the 2PT method. This work was supported by the German Federal Ministry of Education and Research through the BMBF-project "GEP – Grundlagen elektrochemischer Phasengrenzen" (Grant No. 13XP5023D), the Deutsche Forschungsgemeinschaft (DFG) through Grant No. SFB-1316 (collaborative research center), as well as through the Icelandic Research Fund under Grant No. 174582-052. Computational resources were provided by the state of Baden–Württemberg through bwHPC and the German Science Foundation (DFG) under Grant No. INST 40/467-1 FUGG. The Volkswagen Group, Wolfsburg, Germany is acknowledged for partial funding of this project.

Conflict of Interest

The authors declare no conflict of interest.

Keywords

electrocatalysis, fuel cells, oxidation, platinum catalysts, ReaxFF

Received: September 10, 2019
Revised: November 17, 2019
Published online: December 26, 2019

[1] F. Cheng, J. Chen, *Chem. Soc. Rev.* **2012**, *41*, 2172.
[2] H. Puliyalil, D. Lašič Jurković, V. D. B. C. Dasireddy, B. Likozar, *RSC Adv.* **2018**, *8*, 27481.
[3] J. Wu, H. Yang, *Acc. Chem. Res.* **2013**, *46*, 1848.
[4] S. Zhang, X.-Z. Yuan, J. N. C. Hin, H. Wang, K. A. Friedrich, M. Schulze, *J. Power Sources* **2009**, *194*, 588.
[5] J. C. Meier, C. Galeano, I. Katsounaros, J. Witte, H. J. Bongard, A. A. Topalov, C. Baldizzone, S. Mezzavilla, F. Schüth, K. J. J. Mayrhofer, *Beilstein J. Nanotechnol.* **2014**, *5*, 44.
[6] A. Morozan, B. Jousselme, S. Palacin, *Energy Environ. Sci.* **2011**, *4*, 1238.
[7] N. Tian, Z.-Y. Zhou, S.-G. Sun, *J. Phys. Chem. C* **2008**, *112*, 19801.
[8] E. Skúlason, A. A. Faraj, L. Kristinsdóttir, J. Hussain, A. L. Garden, H. Jónsson, *Top. Catal.* **2014**, *57*, 273.
[9] G. A. Tritsaris, J. Greeley, J. Rossmeisl, J. K. Nørskov, *Catal. Lett.* **2011**, *141*, 909.
[10] M. Shao, A. Peles, K. Shoemaker, *Nano Lett.* **2011**, *11*, 3714.
[11] P. Strasser, *Science* **2015**, *349*, 379.
[12] J. K. Nørskov, J. Rossmeisl, A. Logadottir, L. Lindqvist, J. R. Kitchin, T. Bligaard, H. Jónsson, *J. Phys. Chem. B* **2004**, *108*, 17886.
[13] V. Stamenkovic, B. S. Mun, K. J. J. Mayrhofer, P. N. Ross, N. M. Markovic, J. Rossmeisl, J. Greeley, J. K. Nørskov, *Angew. Chem.* **2006**, *118*, 2963.
[14] J. K. Nørskov, T. Bligaard, J. Rossmeisl, C. H. Christensen, *Nat. Chem.* **2009**, *1*, 37.
[15] N. Seriani, W. Pompe, L. C. Ciacchi, *J. Phys. Chem. B* **2006**, *110*, 14860.
[16] D. Fantauzzi, S. Krick Calderón, J. E. Mueller, M. Grabau, C. Papp, H.-P. Steinrück, T. P. Senftle, A. C. T. van Duin, T. Jacob, *Angew. Chem., Int. Ed.* **2017**, *56*, 2594.
[17] T. P. Senftle, R. J. Meyer, M. J. Janik, A. C. T. van Duin, *J. Chem. Phys.* **2013**, *139*, 044109.
[18] T. P. Senftle, A. C. T. van Duin, M. J. Janik, *Catal. Commun.* **2014**, *52*, 72.
[19] Software for Chemistry & Materials (SCM), "ReaxFF 2017," http://www.scm.com (accessed: November 2019).
[20] S.-T. Lin, M. Blanco, W. A. Goddard, *J. Chem. Phys.* **2003**, *119*, 11792.
[21] T. Jacob, *J. Electroanal. Chem.* **2007**, *607*, 158.
[22] D. Fantauzzi, J. Bandlow, L. Sabo, J. E. Mueller, A. C. T. van Duin, T. Jacob, *Phys. Chem. Chem. Phys.* **2014**, *16*, 23118.
[23] D. Fantauzzi, J. E. Mueller, L. Sabo, A. C. T. van Duin, T. Jacob, *ChemPhysChem* **2015**, *16*, 2797.
[24] Y. Wen, H. Fang, Z. Zhu, S. Sun, *Phys. Lett. A* **2009**, *373*, 272.
[25] Y. Wen, H. Fang, Z. Zhu, S. Sun, *Phys. Lett. A* **2009**, *373*, 1800.
[26] R. Huang, Y.-H. Wen, Z.-Z. Zhu, S.-G. Sun, *J. Mater. Chem.* **2011**, *21*, 11578.
[27] "Cohesive Energy | The Elements Handbook at KnowledgeDoor," http://www.knowledgedoor.com/2/elements_handbook/cohesive_energy.html (accessed: November 2019).
[28] S. G. Lambie, G. R. Weal, C. E. Blackmore, R. E. Palmer, A. L. Garden, *Nanoscale Adv.* **2019**, *1*, 2416.
[29] T. P. Senftle, M. J. Janik, A. C. T. van Duin, *J. Phys. Chem. C* **2014**, *118*, 4967.
[30] K. Wang, H. Wu, M. Ge, W. Xi, J. Luo, *Mater. Charact.* **2018**, *145*, 246.
[31] G. A. Kimmel, N. G. Petrik, Z. Dohnálek, B. D. Kay, *Phys. Rev. Lett.* **2005**, *95*, 166102.
[32] H.-Y. Park, S. H. Ahn, S.-K. Kim, H.-J. Kim, D. Henkensmeier, J. Y. Kim, S. J. Yoo, J. H. Jang, *J. Electrochem. Soc.* **2016**, *163*, F210.
[33] A. Vegas, *Inorganic 3D Structures*, Springer-Verlag, Berlin Heidelberg **2011**.
[34] G. L. Dimas Rivera, *PhD Thesis*, Universidad Autónoma de Nuevo León, San Nicolás de los Garza, Mexico **2015**.
[35] A. Dreuw, L. S. Cederbaum, *Chem. Rev.* **2002**, *102*, 181.
[36] E. Guilminot, A. Corcella, F. Charlot, F. Maillard, M. Chatenet, *J. Electrochem. Soc.* **2007**, *154*, B96.
[37] "aradi/nanocut," https://bitbucket.org/aradi/nanocut (accessed: November 2019).
[38] A. C. T. van Duin, S. Dasgupta, F. Lorant, W. A. Goddard, *J. Phys. Chem. A* **2001**, *105*, 9396.
[39] K. Chenoweth, A. C. T. van Duin, W. A. Goddard, *J. Phys. Chem. A* **2008**, *112*, 1040.
[40] G. Kresse, J. Hafner, *Phys. Rev. B* **1993**, *47*, 558.
[41] G. Kresse, J. Hafner, *Phys. Rev. B* **1994**, *49*, 14251.
[42] G. Kresse, J. Furthmüller, *Phys. Rev. B* **1996**, *54*, 11169.
[43] G. Kresse, J. Furthmüller, *Comput. Mater. Sci.* **1996**, *6*, 15.
[44] G. Kresse, D. Joubert, *Phys. Rev. B* **1999**, *59*, 1758.
[45] J. P. Perdew, K. Burke, M. Ernzerhof, *Phys. Rev. Lett.* **1996**, *77*, 3865.
[46] D. Gunceler, K. Letchworth-Weaver, R. Sundararaman, K. A. Schwarz, T. A. Arias, *Modell. Simul. Mater. Sci. Eng.* **2013**, *21*, 074005.
[47] K. Mathew, R. Sundararaman, K. Letchworth-Weaver, T. A. Arias, R. G. Hennig, *J. Chem. Phys.* **2014**, *140*, 084106.
[48] K. Mathew, R. G. Hennig, *ArXiv160103346 Cond-Mat* **2016**.
[49] M. Van den Bossche, E. Skúlason, C. Rose-Petruck, H. Jónsson, *J. Phys. Chem. C* **2019**, *123*, 4116.
[50] F. Neese, *Wiley Interdiscip. Rev.: Comput. Mol. Sci.* **2012**, *2*, 73.
[51] F. Weigend, R. Ahlrichs, *Phys. Chem. Chem. Phys.* **2005**, *7*, 3297.
[52] F. Weigend, *Phys. Chem. Chem. Phys.* **2006**, *8*, 1057.
[53] D. Andrae, U. Häußermann, M. Dolg, H. Stoll, H. Preuß, *Theor. Chim. Acta* **1990**, *77*, 123.
[54] A. V. Marenich, C. J. Cramer, D. G. Truhlar, *J. Phys. Chem. B* **2009**, *113*, 6378.
[55] W. Humphrey, A. Dalke, K. Schulten, *J. Mol. Graphics* **1996**, *14*, 33.